Electrocatalysis (2017) 8:540–553
DOI 10.1007/s12678-017-0364-z

ORIGINAL ARTICLE

A Carbon-Free Ag–Co_3O_4 Composite as a Bifunctional Catalyst for Oxygen Reduction and Evolution: Spectroscopic, Microscopic and Electrochemical Characterization

Hatem M.A. Amin[1,2] · **Christoph J. Bondue**[1] · **Santhana Eswara**[3,4] · **Ute Kaiser**[4] · **Helmut Baltruschat**[1]

Published online: 24 March 2017

Abstract A key challenge for rechargeable metal–air batteries is the development of a cost-effective bifunctional catalyst for both oxygen evolution (OER) and reduction (ORR) reactions. Here, we took the advantages of high OER activity of Co_3O_4 spinel and high ORR activity of Ag to develop a carbon-free oxygen electrode, e.g., for Li–air batteries. The optimized Ag + Co_3O_4 catalyst was further characterized and exhibited a good bifunctional activity in alkaline media. From rotating ring-disk electrode results, the mixed Ag + Co_3O_4 catalyst revealed significantly lower (~320 mV) overpotential for ORR than single Co_3O_4, and a slightly lower overpotential than pure Ag. A four-electron pathway was also elucidated. The OER activity of the mixed catalyst is 1.5-fold compared to pure Co_3O_4, although the Co_3O_4 loading is only 10%, suggesting a large synergistic effect. The potential difference between OER and ORR (i.e., the sum of the overpotentials at 1 mA cm^{-2}) is ca. 0.85 V, which is comparable to noble metal based catalysts. To better understand the origin of this synergism, an XPS analysis was performed, demonstrating that only after oxidation of the mixed catalyst, Co_3O_4 was reduced to $Co(OH)_2$ at potentials of the ORR, probably due to the presence of Ag^+. This redox switching, which was not observed for pure Co_3O_4, is a probable explanation for the increased catalytic activity. The morphology and the electrochemically active surface area of Ag on the surface were examined by electron microscopy and lead-underpotential deposition, respectively. These results also show that when 88% of the Ag surface is blocked by Co_3O_4 particles, the residual 12% free Ag sites altogether have a higher activity for ORR than the (100%) pure Ag surface, i.e., the activity per Ag site is increased by more than a factor of 10. The combination of low cost and high performance endows this catalyst as a promising candidate for energy devices, and the present synergistic effect opens a new track for high activity.

Keywords Silver-cobalt oxide · Oxygen reduction reaction · Oxygen evolution reaction · Underpotential deposition · XPS

Electronic supplementary material The online version of this article (doi:10.1007/s12678-017-0364-z) contains supplementary material, which is available to authorized users.

✉ Helmut Baltruschat
baltruschat@uni-bonn.de

Hatem M.A. Amin
hatem@pc.uni-bonn.de

[1] Institute of Physical and Theoretical Chemistry, University of Bonn, 53117 Bonn, Germany

[2] On leave from Department of Chemistry, Faculty of Science, Cairo University, Giza 12613, Egypt

[3] Present address: Materials Research and Technology Department, Luxembourg Institute of Science and Technology, L-4422 Belvaux, Luxembourg

[4] Central Facility of Electron Microscopy, University of Ulm, 89081 Ulm, Germany

Introduction

Today's energy demand has stimulated scientists to focus on research for developing feasible energy conversion/storage systems. Among the numerous electrochemical devices, regenerative fuel cells and rechargeable metal–air batteries are considered very promising systems for future applications, particularly for automobile industry. For instance, rechargeable Li-O_2 batteries would have less weight, less cost, and higher theoretical energy density than the state-of-the-art Li–ion batteries [1]. The use of an oxygen electrode in an aqueous electrolyte Li–air battery should be possible if the Li electrode is protected by a Li^+–ion conducting membrane [2]. OER and

ORR are at the heart of these technologies and thus of prime importance. However, one of the main obstacles that face the commercialization of such energy devices is the sluggish kinetics of OER and ORR, which leads to higher charge-discharge overpotential and lower efficiency [3]. Therefore, an efficient bifunctional catalyst is indispensable to improve the activity, reversibility, and durability of the O_2 electrode and to reduce the overpotential and total cost.

Pt-based materials are the most conventional catalysts for ORR in alkaline and acidic media [4–7]. Furthermore, other noble metals such as Ru-based materials were investigated and found to be ORR efficient and methanol tolerant catalysts (e.g., RuSe) [8, 9]. However, the high cost, sensitivity to contaminants, and deficiency in resources of Pt limit its large-scale application. Hence, numerous efforts have been done to develop cost-effective catalysts. One approach, mostly applied in acidic media, is reducing the Pt loading through alloying with transition metals like Co [10] or Ni [11], or by control of the size of Pt [12], or by using the core–shell architecture as in the case of Ni@Pt [13]. Another effective approach is to combine noble metals with transition metal oxides. For example, a synergistic bifunctional activity has recently been reported for a mixture of Pt/C and perovskite/C with outstanding electrocatalytic activity [14]. However, this composite is still not cost-effective for large-scale applications. As an alternative, noble metal-free materials based on transition metal oxides or perovskites have been examined [15–18]. Also, metal oxides and perovskites have been combined with non-noble metals (e.g., Ag) and showed good bifunctionality [19–22]. Cobalt oxide-based electrodes were reported as bifunctional catalysts and showed good activity [23–25]. However, they are typically loaded on a carbon support [24, 25], which suffers from corrosion problem. Recently, it was shown that the state-of-the-art Pt/C exhibited severe degradation in alkaline media (three times worse than in acidic) [26], and the cycle life of the carbon-based electrode was limited by the corrosion/oxidation of carbon rather than the catalyst under anodic conditions [27]. Thus, one of the milestones in air electrodes is to develop an efficient carbon-free bifunctional catalyst for both ORR and OER with high stability. Cobalt oxide has high activity and stability toward OER; however, it is less active for ORR [28]. On the other hand, silver is a promising material to replace Pt due to its relatively low cost, high crustal abundance, well-known kinetics, and high ORR activity [29–31]. However, it is less active and not stable for OER.

Thus, the idea followed here is to combine the benefits of a highly conductive silver catalyst (active for ORR) with those of Co_3O_4 (highly active for OER) in one mixture. Ag acts also as a support instead of the carbon particles. Few previous reports have discussed carbon-free catalysts; however, either they showed higher overpotential for OER/ORR or the steady-state data and durability tests are absent [32–34]. One report has demonstrated the design of an Ag–Co surface alloy, but showed only its ORR application [35]. Recently, we have reported a good bifunctional catalyst, which is prepared by simple mixing of Co_3O_4 and Ag particles [36]. Although this is not a surface alloy, the resulting catalyst even shows a synergistic effect between the two components: it is better for both OER and ORR than its constituents, i.e., Co_3O_4 or Ag [36]. An optimization of the ratio of the two components has also been performed in our previous reports [36, 37]. The optimized composite was as well tested in a gas diffusion electrode and analyzed by XRD [37, 38]. It is the aim of this paper to further characterize this bifunctional catalyst and to better understand the origin of the synergistic effect using X-ray photoelectron spectroscopy (XPS).

Furthermore, one of the fundamental issues in catalyst characterization is the determination of the electrochemically active surface area (ECA) of the catalyst, since there is no straightforward and standard method for all non-platinum catalysts. Pb-under potential deposition (Pb-UPD) method has been applied for Ag-based catalysts [39–41]. Therefore, a similar procedure is applied here for ECA estimation of Ag in the mixed catalyst in LiOH media. Moreover, the morphology is examined with electron microscopy. To monitor the intrinsic catalytic activity of the catalysts, and decouple it from mass-transport loss, rotating ring-disk electrode (RRDE) technique was used. By RRDE technique, stationary measurements under controlled mass-transport of the electrochemically active species (oxygen) in the electrolyte were conducted. The effect of catalyst loading on the activity of ORR/OER was also investigated. In order to understand the changes in surface chemistry under different reaction conditions, we identified the electrochemical features using cyclic voltammetry (CV) and simultaneously probed the surface oxidation states of the catalyst using XPS. Also, an elucidation of the (possible routes of the) synergistic interaction between Ag and Co_3O_4 was achieved by XPS analysis. The catalytic activity and stability of this mixed catalyst suggest one of the most non-precious and highly efficient catalysts in alkaline media to date.

Experimental

Electrode Preparation

Silver microparticles (Ag311) (Ferro GmbH) and spinel Co_3O_4 nanoparticles (50 nm, 99.5%, Aldrich) were used as components of our mixed catalyst. Ag311 and Co_3O_4 powders were used as provided. Chemicals used are listed with details in the supporting information. The bimetallic catalyst was loaded on a glassy carbon (GC) substrate. The GC electrodes (0.196 cm^2) were polished to a mirror finish prior to use: first with the help of 0.05 μm alumina slurry on a polishing cloth

(Microcloth PSA 2, Buehler), and then the GC electrodes were cleaned from the suspension residues and adhering impurities with acetone (99.5%, Sigma-Aldrich) and Milli-Q water. Finally, the electrodes were cleaned with Milli-Q water in an ultrasonic bath (VWR®, Germany) for 5 min and afterward dried with Kimtech wipes and coated with the respective catalyst ink. The procedure for preparing the catalyst modified-GC electrode was mentioned in our previous paper [36]. Briefly, the catalyst suspension was prepared by dispersing an appropriate amount of the catalyst powder (Co_3O_4 or Ag311 or their mixture) in ethylene glycol (EG) using ultrasonic path for 40 min (10 mg powder in 5 ml EG). For the mixed catalyst, both powder components were physically mixed in EG, where 10 wt% Co_3O_4 was used. Next, 20 μl of the catalyst suspension was drop-cast onto the surface of the GC electrode by Eppendorf-pipette, yielding the required loading (200 μg cm^{-2}), and then dried for 10 min at 190 °C in an oven. Afterward, 20 μl of Nafion® solution (1.44 mg Nafion in 1 ml water) was pipetted onto the catalyst to fix it on GC. Higher loadings were prepared from the same ink solution. For 1 mg cm^{-2} loading, the catalyst addition was repeated five times or in the case of Ag311 two additions from a concentrated ink containing 10 mg catalyst in 2 ml EG were done. The electrode was dried again at 190 °C. After cooling the electrode, the distribution of the particles on the surface of GC was checked by an optical microscope and finally installed in the measuring setup. Nafion layer thickness (20 μl used for all catalysts) was made sufficiently thin (less than 0.2 μm as calculated from a covered electrode area of 0.196 cm^2 and apparent film density of 2.0 g cm^{-3}) so that the film diffusion resistance becomes negligible [42].

The loading of the catalyst was chosen such that the thickness of the catalyst does not exceed one layer of the Ag particles. Using a simple ball model, 1 mg cm^{-2} of Co_3O_4 (50 nm) would correspond to about 50 monolayers of Co_3O_4 particles, and considering thickness of ~0.2 nm for monolayer, one could get ~10 nm thickness. In addition, we have examined, by an optical microscope, different loadings, and we found that with lower loadings, the surface of GC is not completely covered. Thus, we chose in this study 1 mg cm^{-2} loading.

Electrochemical Characterization

RRDE and CV measurements were conducted in a three-electrode glass cell using a rotor and a Pine Bipotentiostat (AFCBP 1, Pine Research Instrumentation, USA and has a built-in function generator). The catalyst-coated GC disk (5 mm diameter) was employed as the working electrode (WE). The disk was surrounded radially by a Pt-ring of 6.5 mm internal diameter and 7.5 mm outer diameter and was mounted to the RRDE Teflon Tip. Prior to use, the ring electrode was polished with 0.05 μm alumina slurry and rinsed with Milli-Q water. The counter electrode was a Pt sheet immersed in a glass tube connected to the cell via a glass frit. The reference electrode was a reversible hydrogen electrode (RHE) in the base electrolyte and was placed very close to the WE via a Luggin capillary. A LabVIEW software (National Instruments GmbH, Munich, Germany) was used for data collection. The lower cycling potential limit was chosen as −0.2 V vs. RHE to reduce any Ag species in the catalyst. The ring potential was kept constant at 1.2 V (vs. RHE). The electrolytes were continuously purged with O_2 or Ar before and during the measurements. All experiments were conducted at room temperature, 25 ± 1°. Pb-UPD experiments were carried out in a separate three-electrode glass cell to avoid any Pb contamination that might affect the activity. Pb-UPD was conducted in 0.1 M LiOH containing 125 μM $Pb(NO_3)_2$ and by holding the potential at 0.24 V (vs. RHE in 0.1 M LiOH) for 180 s and then sweeping to 0.7 V (vs. RHE) at 100 mV s^{-1}. The anodic stripping voltammograms were then integrated to estimate the surface area. Details of RRDE calculations are given in the supporting information.

Surface and Spectroscopic Characterization

The morphology of the catalyst was examined by scanning electron microscope (SEM) at Ulm University (Zeiss Dual-Beam NVISION 40 with an operating voltage of 5–30 kV). The energy-dispersive X-ray (EDX) data were obtained using AMETEK EDAX, type Genesis APEX2.

XPS spectra were collected in the main chamber of a UVH-system with an attached Omicron EA125 hemispheric electron energy analyzer and an X-ray tube with a magnesium anode. Schematic illustration of the electrochemical-XPS instrument is shown in Fig. S1. After conducting the electrochemical experiment in the ante-chamber, the electrolyte was replaced with 10^{-4} M LiOH solution. The electrode was dipped into this solution under potential control for several times in order to remove excess amounts of conducting salt, which would cover the electrode, after the solvent was evaporated under ultrahigh vacuum (UHV) conditions [43]. The manipulator facilitates positioning of the working electrode during electrochemical measurements in the ante-chamber and the XPS in the main chamber (see details in the supporting information). Due to stepper motors at the manipulator, it was possible to approach the identical position in each experiment.

Results

Electrochemical Performance of the Catalyst

To evaluate the electrocatalytic activity of the mixed Ag311 + Co_3O_4 catalyst and its single components for ORR, RRDE tests were conducted in O_2-saturated 0.1 M LiOH solution at

a rotation rate of 960 rpm and a scan rate of 10 mV s^{-1}, see Fig. 1a. The same mass loading of 1 mg cm^{-2} for all catalysts was used. ORR showed no obvious current plateau at Co_3O_4, while a wide current plateau was witnessed at the other catalysts. However, the diffusion-limited currents should theoretically coincide for the various catalysts (theoretically 3.6 mA cm^{-2} at 960 rpm for 4e-process), but practically, they do not: because of the low loading, parts of the electrode remain uncovered by catalyst so that the GC substrate contributes. The shape of the CV for the mixed catalyst is more similar to that of Ag because the proportion of Ag in the composite was larger. The redox peaks in the polarization

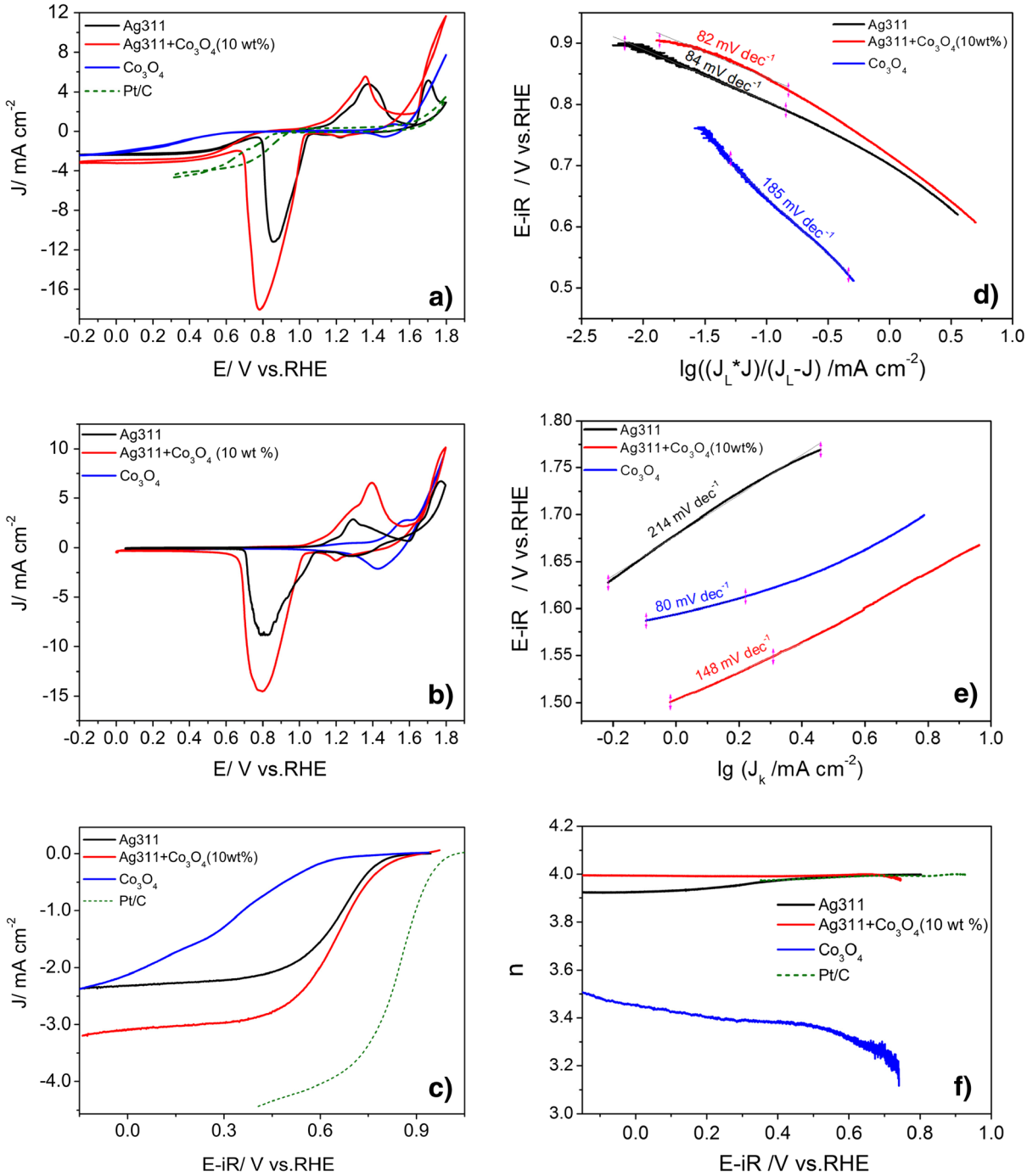

Fig. 1 **a** CV curves on Ag311, Ag311 + Co_3O_4(10 wt%), Co_3O_4 and Pt/C catalysts (1 mg cm^{-2}) on GC electrode in O_2-saturated 0.1 M LiOH solution at a rotation rate of 960 rpm with a scan rate of 10 mV s^{-1}. **b** Polarization curves of various catalysts in Ar-saturated 0.1 M LiOH solution with a scan rate of 50 mV s^{-1}. Catalysts in **a** and **b** are different preparations. **c** iR and capacitive current-corrected polarization curves derived from anodic scan in **a**. The corresponding mass-transport corrected Tafel plots **d** for ORR and **e** for OER. **f** Electron transfer number (*n*) derived from the corresponding RRDE data in **c** at various potentials

curves are due to the different oxidation and reduction states of Ag and Co and their oxides and also seen in Ar-saturated electrolyte, Fig. 1b. Ag oxidation and reduction is a reversible process. Although the peak at ca. 1.3 V in Fig. 1b is not identical in intensity to that in Fig. 1a, it is always higher in presence of Co_3O_4 in the mixture. The rate of ORR is given by the current in the anodic sweep, which is not influenced by the surface redox processes. Figure 1c shows the curves for ORR after correction for the iR-drop and the capacitive current. ORR was observed at lower overpotentials and with higher currents at the mixed 10% catalyst compared to the pure components (20 mV vs. Ag and 330 mV vs. Co_3O_4 at 1 mA cm^{-2}), see Fig. 1c. For ORR, the half-wave potential of the Ag311 + Co_3O_4 (10 wt%)mixed catalyst was similar to that at Ag and about 350 mV more positive than that at Co_3O_4, but about 200 mV less positive than that at Pt/C, indicating a good activity for ORR. The current density of the mixed catalyst at 0.7 V was 1.3 times higher than that at pure Ag catalyst (0.93 compared to 0.71 mA cm^{-2}, respectively).

For OER, our previous report showed that the current in the negative-going scan corresponds to OER activity, whereas the positive-going scan is dominated by the formation of silver oxide [36]. The steady-state experiments (done for 3 min) revealed that the currents are mostly stable for the mixed and pure Co_3O_4 catalysts, but not for pure Ag [36]. For OER, the onset potential of the mixed catalyst was the same as that of Co_3O_4 (ca. 1.55 V); however, it showed current improvement by about 150% compared to Co_3O_4 at 1.8 V. Pure Ag311 showed a negligible activity to OER. For comparison, a Pt/C catalyst was tested. The mixed catalyst showed superior activity for OER compared to the commercial Pt/C, see Fig. 1a. The potential gap between ORR and OER was about 0.85 V at 1 mA cm^{-2} for both reactions at the mixed catalyst.

Tafel plots (currents were corrected for diffusion, see details in the "Experimental" section) of the corresponding curves of Fig. 1a are shown in Fig. 1d, e for ORR and OER, respectively. Interestingly, Ag and the mixed catalysts showed similar Tafel slope for ORR (82 mV dec^{-1} at lower overpotentials 0.8–0.9 V), whereas a higher value (ca. 185 mV dec^{-1}) was obtained for Co_3O_4, suggesting that the catalytic performance for ORR is dominated by Ag in the mixed catalyst. Tafel slope at Ag is in agreement with literature values (80 mV dec^{-1}) for Ag(110) [30] and Ag particles [44]. Indeed, Ag exists at OER potentials as Ag-oxide and is reduced at lower potentials to metallic Ag, which is effective for ORR. For OER, Tafel slopes of about 80, 210, and 150 mV dec^{-1} were obtained at lower potentials for Co_3O_4, Ag, and mixed catalysts, respectively. The Tafel slope for Co_3O_4 is close to reported values (65–75 mV dec^{-1}) [28, 45]. Also, similar Tafel slope of 183 mV dec^{-1} was obtained at higher potentials for both Co_3O_4 and the mixed catalyst, implying that Co_3O_4 is the dominant component in OER activity in the mixed catalyst. This assesses the interplay between Ag and Co_3O_4 in their mixture in the two different processes. Also, the overall number of electrons transferred (n) was determined from the ring currents and found to be 3.9–4.0 for both Ag311 and the mixed 10% catalysts over the potential range of ORR and ~3.5 for the spinel Co_3O_4, Fig. 1f. Therefore, ORR on the mixed catalyst follows the four-electron pathway with negligible peroxide formation. Moreover, ORR is controlled by diffusion of O_2 to the electrode surface since the dependence of current density on the rotation rate (i.e., Koutecky-Levich (K-L) plots, not shown) reveals a straight line passing through the origin. All of the above evidence that the activity was improved by a synergistic effect between Ag and Co_3O_4.

Long-term stability measurements have been done in our previous report on a GDE for the same catalysts and showed good durability for 200 successive cycles at OER and OER potentials [37]. Only a slight decay of current was observed in the first 50 cycles of OER, but it remains stable afterward. For model electrodes such as those used in this study, the quasi steady-state currents for ORR were only slightly less than the currents in the cathodic-going scan in the CV [36]. This was obtained by holding the potential for few minutes at different potentials and recording the current. For OER, Ag-containing catalysts exhibited current decay in the first minute where the high current involves the continuation of Ag-oxide formation, and then stable currents were obtained for pure OER. Co_3O_4 and the mixed catalysts showed good stability after 1 min, and the very small decay is due to blocking of some active sites with evolved oxygen bubbles. In contrast, Ag catalysts showed large decay and less activity for OER [36, 37]. For ORR, there is no significant decay in current in the potentiostatic experiment.

Surface Characterization

Furthermore, the morphology and distribution of the catalyst were examined by SEM. To get better resolution for SEM, we also imaged the surface without Nafion (Fig. 2a) in addition to the one containing Nafion before electrochemical processes (Fig. 2b). In Fig. 2a, the composite consists of particles of two different contrasts. The individual Co_3O_4 particles can be clearly identified as bright spots with ca. 50 nm size partially covering (and attached to) the darker 1 μm Ag particles. The identification of the particles has been achieved by EDX data on the same catalyst in our previous report [36]. Co_3O_4 nanoparticles are dispersed as a 2D layer on the larger Ag particles; 3D agglomerates are not observed (Fig. 2b). Therefore, the larger Ag particles seem to be covered by a porous layer of the Co_3O_4 nanoparticles. The catalyst with Nafion shows slightly blurred images. The coexistence of Co_3O_4 in contact with Ag seems to provide stable anchor sites to keep the particles separated and prevent migration and coalescence during electrochemical cycling.

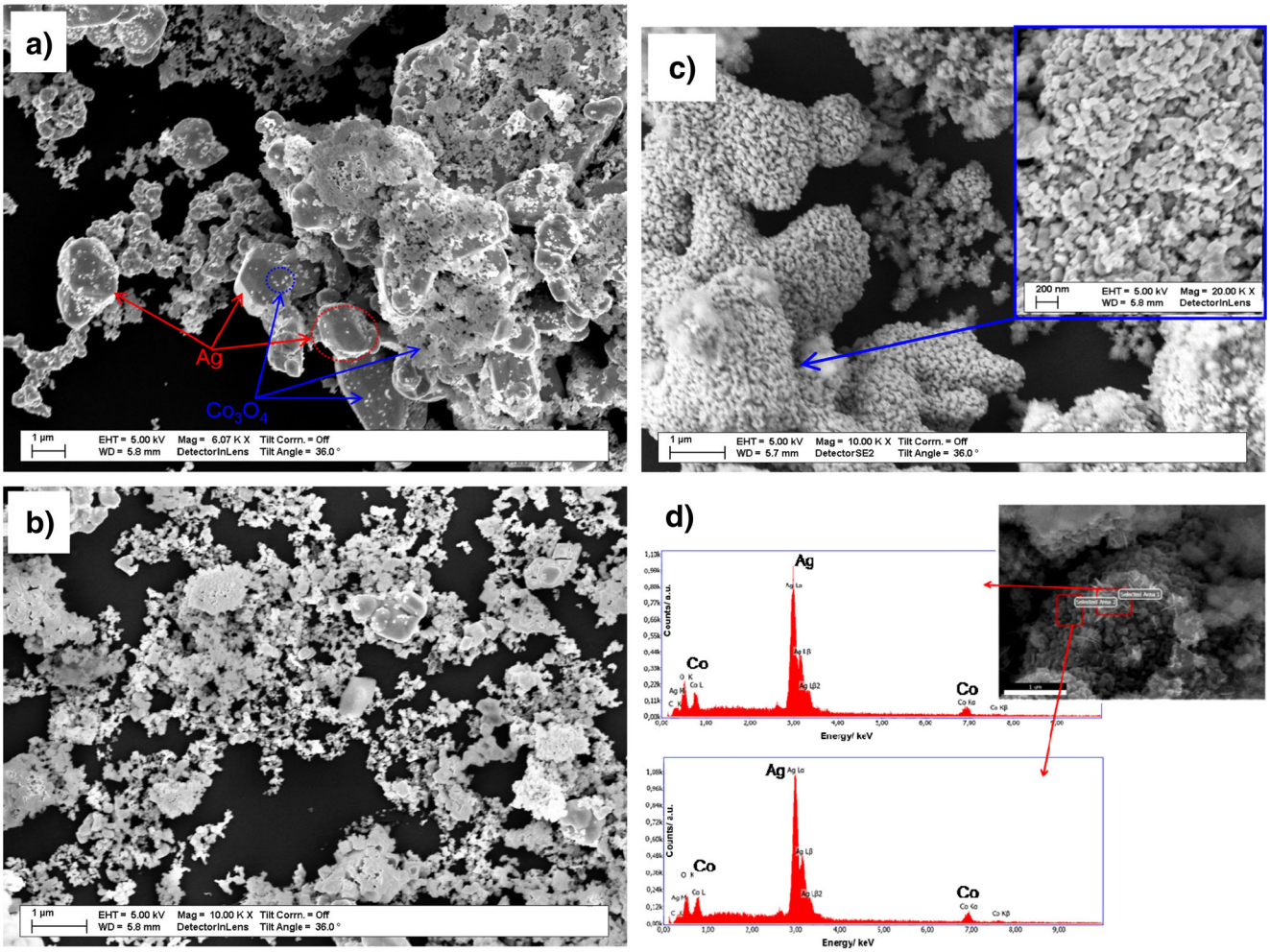

Fig. 2 SEM images of the 1 mg cm^{-2} mixed Ag + Co_3O_4 (10 wt%) **a** without Nafion and **b** with Nafion before OER/ORR cycling, while **c** with Nafion emersed at 1.0 V after cycling (oxidation and reduction). The *inset* is a zoom-in of part of the surface. **d** EDX spectra of a part of the surface of the mixed catalyst after several ORR/OER cycles

Therefore, exposing the appropriate loading of the catalyst on GC does not induce significant mobility of the particles on the surface. SEM micrograph of the mixed catalyst with Nafion after several OER and ORR cycles (40 cycles) and the electrode was emersed at 1.0 V in the cathodic direction is shown in Fig. 2c. After oxidation and reduction of the mixed catalyst, larger structures are noticed (ca. 100 nm), which cover most of Ag particles, see the inset of Fig. 2c. These morphological changes, which are observed on the surface after ORR/OER cycles, might be due to an enhanced roughness of the surface linked to Ag oxidation, which also will lead to a stronger contact of the Co_3O_4 nanoparticles with Ag. However, for pure Ag particles, we observed by a simple optical microscope that the particles tend to agglomerate to some extent on the surface (photos are not shown). EDX spectra showed the coexistence of Ag and Co_3O_4 after several cycles, and it seems that large particles are thoroughly covered by small particles, as shown in Fig. 2d. It is possible that rearrangement and growth of Ag occur with partial encapsulation of Co_3O_4 in it.

In order to examine the catalyst more closely, pseudo in situ XPS measurements of the 10% mixed catalyst and of the Co_3O_4 particles alone were performed. For technical reasons, a polycrystalline Ag substrate was used in both cases instead of GC; the total catalyst loading was 400 µg cm^{-2}. In the case of the pure Co_3O_4 catalyst, which will be discussed first, the amount of Co_3O_4 corresponds roughly to 20 layers of nanoparticles (assuming spherically shaped Co_3O_4 particles forming a close-packed layer). Since the investigation of the Ag/Co_3O_4 surface would be impossible if it was covered with a Nafion binder, the nanoparticles were deposited from a suspension in water. Therefore, the particles stuck to the surface of the silver electrode by adhesion only. Figure 3d displays the CV of this electrode and indicates the sequence of the experiments: in each experiment, the electrode was immersed at 0 V into an electrolyte of 0.1 M LiOH and cycled to the indicated potential. In the first (black curve in Fig. 3) and in the third

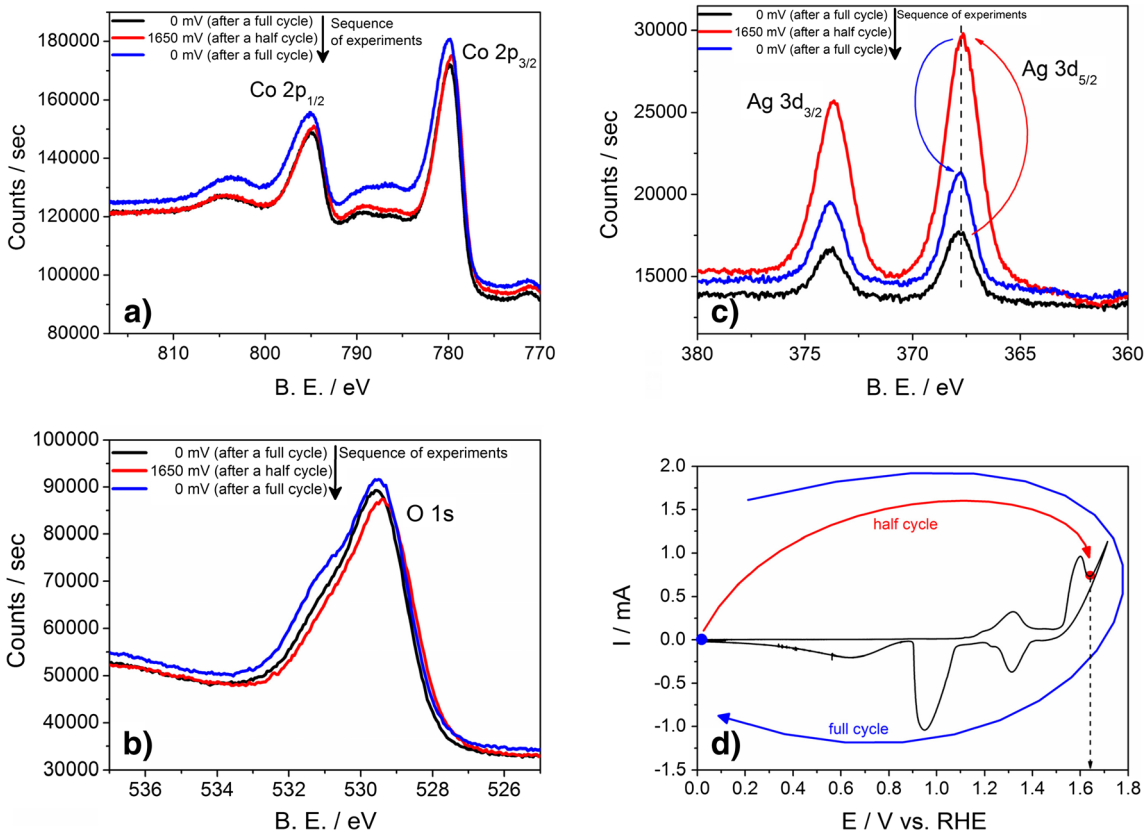

Fig. 3 XP-spectra of Ag (pc) electrode covered with 400 μg cm^{-2} Co_3O_4 nanoparticles after electrochemical polarization to the indicated potentials (vs. RHE) in an electrolyte of 0.1 M LiOH. **a** Co 2p-lines. **b** O 1s-line. **c** Ag 3d-lines. **d** CV of this electrode. The experiment was conducted as indicated: Starting from 0 V, the electrode was cycled to either 1.65 V or back to 0 V where the transfer to the UHV chamber was conducted. Sweep rate = 5 mV s^{-1}

(blue curve in Fig. 3) experiment, the electrode performed a full cycle in the potential range from 0 to 1.70 V. The electrode was then emersed at 0 V and transferred to the main chamber, where the XP-spectrum was collected. In the second experiment, only a half cycle was performed, and the electrode was emersed at 1.65 V.

Figure 3 shows the highly resolved XP-spectra of the Co 2p-line (Fig. 3a), the O 1s-line (Fig. 3b) and the Ag 3d-line (Fig. 3c). According to the Pourbaix diagrams published by Chivot et al. [46], cobalt forms either Co_3O_4 or CoO(OH) at 1.65 V. Although the positions of the Co 2p-lines (at around 780 and 795 eV) are not very sensitive to the oxidation state of cobalt, the shown spectra are assigned to the Co_3O_4 phase as they resemble those spectra shown by Biesinger et al. for Co_3O_4 [47]. This phase was identified by the faint shake-up satellites of the 2p-lines (at around 804, 789, and 786 eV), which are somewhat different in shape for CoO(OH) [48]. In addition, the O 1s line in Fig. 3b points to the presence of Co_3O_4 rather than CoO(OH). Although the line position of the O 1s line is at 529.5 eV and thereby shifted by 0.5 eV to lower binding energies than that reported by Yang et al. for Co_3O_4 [48], it is still a single peak rather than an unresolved doublet, which is expected for CoO(OH) [48]. It also does not change with potential. Strasser and coworkers also found (by XRD and XPS, in a neutral electrolyte) crystalline Co_3O_4 both at 1.2 and 1.62 V (vs. RHE); at the higher potential, which corresponds to the onset of OER, only the outermost surface is partially oxidized to $CoO_x(OH)_y$ [45]. The formation of silver oxide at high potentials does not affect the shape or position of the O 1s peak because the surface is largely covered by Co_3O_4 nanoparticles. Thus, the XP-spectra in Fig. 3 show that Co_3O_4 is present at the surface both at 1.65 and at 0 V. From thermodynamics, it is expected that the Co_3O_4 particles do not undergo any phase transition at 1.65 V [46]. However, at 0 V, no $Co(OH)_2$ was formed although this would be the stable phase according to the Pourbaix diagram of cobalt at this potential [46].

The positions of the Ag 3d-lines remain unaltered regardless of the applied potential. In a control experiment, a blank Ag (polycrystalline) electrode has been polarized in the same electrolyte to several potentials in the absence of any Co_3O_4. The XP-spectra of the Ag-3d and the Ag MNN Auger lines as well as that of the O 1s-line can be found in Figs. S2 to S4 in the supporting information. As mentioned above, the prominent peaks in the anodic direction at 1.3 and 1.6 V (see Fig. 3d) are due to the oxidation of silver [36]. These

experiments showed that the Ag 3d-lines are insensitive to the oxidation state of silver. This finding is in contrast to an earlier report, where the authors found a decrease of the binding energy upon oxidation of silver [38]. However, a reduced binding energy at higher oxidation states is rather unusual. Nevertheless, we can observe changes in the less intense Ag MNN lines, which indicate the formation of Ag_2O in the first oxidation peak (at 1.3 V). The Ag MNN lines were not investigated in [38]. Further changes in the Ag MNN lines did not appear as the potential is increased to 1.72 V, where AgO is formed [49] (i.e., more precisely $Ag^{I}Ag^{III}O_2$ since $Ag^{II}O$ is not known to exist [36, 38, 50]). Regardless of the actual product of oxidation at 1.72 V, we assume that this product is not stable under UHV conditions where the oxygen partial pressure is approaching zero. This is supported by the fact that the open circuit potential of the electrode after its back transfer is at 1.12 V, and therefore, more cathodic than 1.30 V where a peak due to the reduction of $Ag^{I}Ag^{III}O_2$ appeared. However, regardless of the oxidation state of the polycrystalline silver, the intensity of the Ag 3d lines remained unaltered in all control experiments.

In Fig. 3, the overall intensity of the Ag-lines is very low, as most of the silver surface was covered with Co_3O_4 nanoparticles. However, when the electrode was transferred after polarization to 1.65 V, the intensity was increased compared to the experiment where the electrode was transferred after polarization to 0 V. In order to quantify the effect, the relative atom-% for cobalt, silver, and oxygen was calculated according to Eq. (1) [51] and is listed in Table 1.

$$W_X = \frac{I_x \Big/ \mathrm{ASF}_x}{\sum_i I_i \Big/ \mathrm{ASF}_i} \tag{1}$$

In Eq. (1), W_x is the portion of the element in question in the surface. I_x is the intensity of the respective line in the XP-spectrum as determined by integration after baseline subtraction which needs to be weighted by the atomic sensitivity factor (ASF_x). The weighted signal intensity is divided by the sum of the weighted intensity of all elements in the surface.

According to Table 1 (upper section) for the Co_3O_4 catalyst on Ag (pc), the relative amount of Ag in the surface is low at all potentials; however, it increases significantly, when the electrode is polarized to 1.65 V. Although the formation of silver oxide is expected at this potential, this has little influence on the overall intensity of the oxygen O 1s line as the relative amount of silver oxide in the surface is low. The process that leads to the increased amount of silver in the surface is at least partially reversible. This is shown qualitatively by the blue curve in Fig. 3 and quantitatively by the relative atom-% of silver in the surface listed in Table 1. An increased intensity of the Ag 3d lines means that more silver is exposed to the spectrometer: the volume expansion of Ag_2O during oxidation that pushes more silver through the overlayer of Co_3O_4 particles to the surface is the most probable explanation and is supported by the SEM data shown above.

The contact area between silver and Co_3O_4 is increased in the mixed catalyst. Therefore, the same experiments as shown in Fig. 3 were conducted with an Ag-electrode covered with a mixture of 50 μg cm^{-2} of Co_3O_4 nanoparticles and 400 μg cm^{-2} of Ag311 particles (Ag311 + Co_3O_4 (~10 wt%))/Ag. The resulting XP-spectra are shown in Fig. 4. In this experiment and in contrast to the pure Co_3O_4 catalyst, no significant changes in the Ag 3d intensity appear. Given that already most of the exposed material is silver, this is expected.

From the XP-spectra in Fig. 4a, it is clear that the Co 2p peaks are shifted to a lower binding energy, and the shake-up satellites change both their form and intensity as the electrode was polarized to 0.02 V compared to the spectra which were obtained after polarizing to 1.65 V. While at 1.65 V Co_3O_4 is still present, the spectra obtained at 0.02 V resemble those shown by Biesinger et al. for the CoO or the $Co(OH)_2$-phase [47]. This is different from the experiment, where a polycrystalline silver electrode was covered with Co_3O_4 at all potentials (c.f., Fig. 3a): irrespective of the applied potential, no reduction of the spinel occurred. However, when the electrode was only dipped into the electrolyte at 0.02 V without ever

Table 1 Relative atom-% of oxygen, cobalt, and silver in a surface of a polycrystalline silver electrode covered with either 400 μg cm^{-2} of Co_3O_4 nanoparticles or 400 μg cm^{-2} of Ag311 + 50 μg cm^{-2} of Co_3O_4 after polarization to various potentials

	Rel. atom-% oxygen (theo.)	Rel. atom-% cobalt	Rel. atom-% silver
Co_3O_4/Ag (pc)			
1st full cycle	67.1 (44)	31.9	1.1
Half cycle	61.0 (47)	34.6	4.3
2nd full cycle	62.4 (48)	36.3	1.3
Ag311 + Co_3O_4 (~10 wt%) /Ag (pc)			
1st full cycle	36.5 (34.6)	17.3	46.2
Half cycle	39 (37)	9	52

The values were calculated according to Eq. (1). The required values were obtained by integration of the curves shown in Figs. 3 and 4 after baseline subtraction

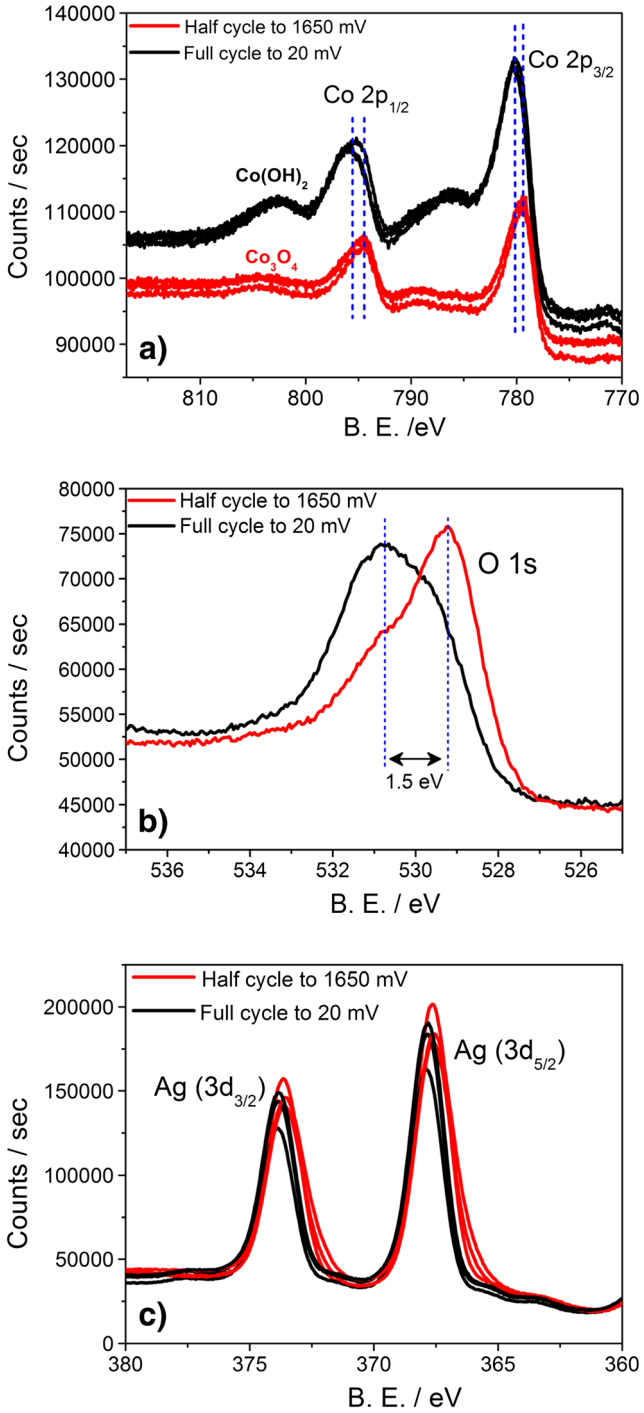

Fig. 4 XP-spectra of an Ag (pc) electrode covered with 50 μg cm^{-2} Co_3O_4 nanoparticles + 400 μg cm^{-2} Ag311 particles after electrochemical polarization to the indicated potentials (vs. RHE) in an electrolyte of 0.1 M LiOH. **a** Co 2p-lines. **b** O 1s-line. **c** Ag 3d-lines. Both for silver and cobalt, three spectra were collected at each potential. The spectra were collected on a rotating basis, after polarizing to 0.02 and 1.65 V, respectively

being polarized to 1.65 V in a previous experiment, the observed Co_3O_4 phase was not reduced (c.f., Fig. S5 of the supporting information). Once the electrode was polarized to 1.65 V, the formation of a Co(II)-phase was observed at 0.02 V. This process is reversible as shown by the switching between the phases in the six spectra for cobalt and silver in Fig. 4a, c. After polarization to 0.02 V, both Ag_2O and Co_3O_4 are reduced. Any oxygen left on the surface belongs to the reduced Co/O-phase, and the O 1s-line at 530.7 eV provides information on the nature of the reduced Co/O-phase: the observed value of 530.7 eV is close to the value of 531.07 eV reported for $Co(OH)_2$ by Biesinger et al., whereas the reported value for the O 1s-line in CoO is 529.79 eV [47]. Hence, at 0.02 V, Co_3O_4 is reduced to $Co(OH)_2$ rather than CoO. This is supported by the oxygen content (cf., Table 1), which is twice the value of Co.

It is clear from the CV in Fig. 2d and the XP-spectra of the Ag MNN lines in Fig. S3 that the silver surface is oxidized at 1.65 V. From the curves shown in Fig. 4, the relative atom-% were calculated according to Eq. (1) for the mixed catalyst and are also listed in Table 1 (lower section). At 1.65 V, the relative cobalt content in the surface is 9%, while that of silver is 52%. A relative oxygen content of 39% ((4/3) × 9% + (1/2) × 52%) at a potential where Co exists as Co_3O_4 is only explicable when Ag is oxidized to Ag_2O. The XP-spectra of the O 1s-line obtained at this potential should reflect the oxidation state of silver since two thirds of the oxygen should exist as Ag_2O. Indeed, the O 1s line of the oxidized surface is located at 529.2 eV in Fig. 4b. This is close to the O 1s line position of 529.5 eV expected for Ag_2O [52]. Since this value is close to that reported for Co_3O_4 (530 eV [47]), it is not expected that the difference between the oxygen atoms in both phases is resolved. However, the O 1s-line of the oxidized surface in Fig. 4b is shifted by 0.3 eV to lower binding energies as compared to the O 1s-line in Fig. 3b where Co_3O_4 is the dominant phase in the surface.

As compared to the reduced surface, the relative cobalt content is reduced by half at the oxidized surface. The decrease of the relative cobalt content signifies some shielding by Ag_2O at the high potential, due to the same effect as the increase of the Ag 3d-peaks in Fig. 3c. At 0.02 V, the ratio of oxygen to cobalt is 2:1, which is expected for $Co(OH)_2$. At this potential, silver should not be covered with an oxide overlayer that would contribute to the relative amount of oxygen in the surface.

Co_3O_4 (spinel-type) has a cubic close packed anion lattice, whereas $Co(OH)_2$ crystallizes in the CdI_2-structure, which is a layered and hexagonal structure. Solid-state reactions like these, in general, involve large activation barriers. That is why the kinetic stability of the well crystallized Co_3O_4 phase at a potential where CoO or $Co(OH)_2$ would be thermodynamically favored is expected. The kinetic stability of Co_3O_4 at low overpotentials is lifted, when the relative contact area between Ag and Co_3O_4 increases: redox switching is only observed on a silver surface with 50 μg cm^{-2} Co_3O_4 + 400 μg cm^{-2} Ag311. On Ag(pc) covered with only 400 μg cm^{-2} of Co_3O_4, no such effect is observed.

However, since the formation of $Co(OH)_2$ is not observed when the electrode is only dipped at 0.02 V, but requires the polarization to 1.65 V in a previous experiment, the presence of metallic silver is not responsible for the facilitated redox switching of cobalt. Although we cannot offer a concrete mechanism that would explain the observed behavior, the need to polarize to large potentials where oxidation of silver occurs suggests that the presence of silver cations is required in order to reduce the Co_3O_4 phase at low potentials. Previously, the activity of ceramic catalysts for oxidation reactions has been assigned to the ability of the metal cation to change its oxidation state [53–55]. Since the presence of Ag facilitates redox switching in Co_3O_4, this might be the reason for the enhanced activity of the Ag + Co_3O_4 electrode over the pure Co_3O_4 phase for OER.

The increased activity of the Ag + Co_3O_4 catalyst in the oxygen reduction region might as well be due to the formation of silver oxide. Figure 3 shows that at high potentials, the silver signal increases as Ag_2O particles push through the layer of Co_3O_4 particles and thus expands to the surface. After reduction of silver oxide, the silver is distributed differently in the surfaces and has partially buried Co_3O_4 particles as supported by SEM data. Fu et al. showed in a thorough study on the oxidation of CO at a catalyst of FeO_{1-x} islands on Pt(111) that the reactivity of CO linearly depends on the islands' periphery density (e.g., the overall length of the periphery per unit area) since dissociative adsorption of oxygen takes place preferentially at those sites [56]. Furthermore, similar effect of the role of the phase boundary has been shown for hydrogen evolution at Pd-modified gold single crystals [57], for CO-electrooxidation at Ru- and Sn-modified Pt(111) single crystals [58–61] and for ORR [14]. In the same way, the activity of the Ag/Co_3O_4 electrode might depend on the presence of phase boundaries between Ag and Co_3O_4.

ECA Estimation

The electrochemically accessible area of Ag on the catalyst surface was determined by lead-underpotential deposition (Pb-UPD) in a similar procedure to that reported in literature [39–41]. Figure 5 shows the stripping CVs obtained for pure Ag311 and the mixed catalysts with various compositions on GC. A monolayer of Pb is deposited onto the Ag surface at potentials more positive to that expected for equilibrium bulk deposition. To obtain the optimum conditions for monolayer deposition, several stripping experiments have been conducted on Ag electrode by varying the deposition potential (E_d) and time (t_d). E_d of 0.24 V vs. RHE and t_d of 180 s were found to be optimum for our Ag311 and mixed Ag + Co_3O_4 hybrid catalysts, where a maximum stripping charge was reached without any bulk deposition. As shown in the CV_s, the reversible peak in the region from 0.25 to 0.5 V is due to the reduction of Pb^{II} to Pb_{UPD} and oxidation of Pb_{UPD} to Pb^{II} in the

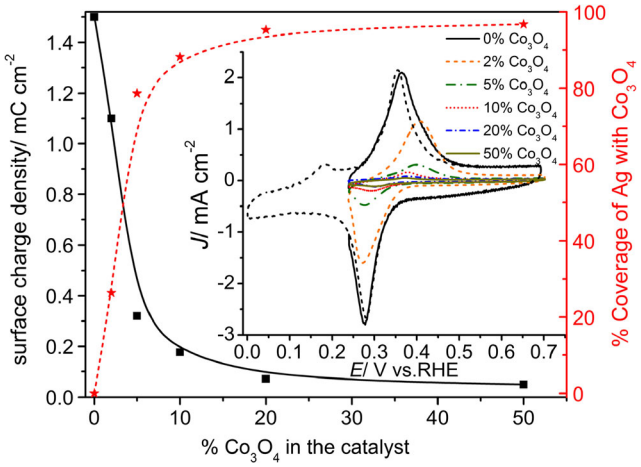

Fig. 5 Results of Pb-UPD on Ag311 + Co_3O_4(10 wt%) in Ar-saturated 125 μM $Pb(NO_3)_2$ + 0.1 M LiOH solution. The *inset* is the stripping CVs obtained at E_d = 0.24 V after t_d = 180 s and with a scan rate of 100 mV s^{-1} (*solid line*), and a consecutive CV with more negative potential limit was recorded for Ag311 (*dashed black line*). Catalyst loading: 1 mg cm^{-2}. The surface charge density was obtained by integration of the anodic stripping peak of the corresponding CV in the inset

cathodic and anodic scans, respectively [40]. Monolayer coverage of Pb_{UPD} requires 260 μC cm^{-2} for a smooth surface [39, 40]. Consequently, for the pure Ag catalyst, a stripping charge density of 1.5 mC cm^{-2} is calculated, which corresponds to an apparent roughness factor of about 6 (i.e., surface area for Ag: ~5.8 cm^2 cm^{-2} geometric area). For the 10% catalyst, the active Ag area is 0.8 cm^2 cm^{-2} geometric area. Scanning to more negative potentials leads to Pb-alloy formation, and an additional anodic peak at 0.2 V, as can be seen in the dashed line of the inset of Fig. 5. Noteworthy, by addition of the Co_3O_4 nanoparticles to Ag in their mixture, the surface area of the Ag particles exposed to Pb-UPD is reduced monotonically, as shown by the reduced stripping charge for Pb (Fig. 5): 88% blocking of the Ag surface area was achieved by addition of 10 wt% of Co_3O_4 in the hybrid, in qualitative agreement with the SEM images shown in Fig. 2. A nearly complete blocking with Co_3O_4 nanoparticles is achieved by dispersion of 20 wt% of Co_3O_4 or more in the catalyst mixture. This is also the composition with a lower ORR activity than Ag.

Moreover, a simple ball model explains this finding: assuming a homogeneous radius of 0.5 μm for Ag particles, the number of particles as well as their total surface area can be calculated, leading to a total surface area of 5.7 cm^2 cm^{-2} of the substrate, in agreement with the above value of 6 for the apparent roughness factor. Similarly, for a uniform diameter of the Co_3O_4 particles, and assuming that each particle blocks a section of $\pi r^2 = \pi(25\ \text{nm})^2$ of the Ag surface (i.e., the area underneath the particles is not accessible), a blocked area of 4.9 cm^2 of Co_3O_4 per square centimeter of the GC substrate is obtained for the 10% Co_3O_4 catalyst, corresponding to 86% of the Ag surface area (to be compared to the experimental value

of 88%). We conclude that a catalyst with an Ag area exposed to the solution of only 12% of that of the pure Ag catalyst showed a higher activity for O_2-reduction than pure Ag. On the other hand, the catalyst with only 10 or 20% Co_3O_4 (which could be thought to be responsible for O_2 evolution) in the mixture has the same (or even a higher) activity than pure Co_3O_4.

Influence of Catalyst Loading and Electrolyte Concentration

The catalyst loading has a strong impact on the detection of HO_2^- at the ring of RRDE and therefore on the catalytic activity and ORR mechanism. Poux et al. have investigated the loading effect on perovskite catalyst and concluded that ORR follows predominantly the series 2e + 2e pathway through formation of HO_2^- intermediate [62]. The extent of escape of this intermediate from the surface depends strongly on the catalyst loading [62]. Here, we investigated the loading effect of the Ag311 + Co_3O_4 (10 wt%) catalyst on GC substrate. Three different loadings of the catalyst on GC were examined, see Fig. 6. The onset and polarization curves of ORR shifted to more positive potentials as the loading increased (Fig. 6a). Noticeably, a decrease in the catalyst loading leads to a decrease in the disk currents, an increase in the ring currents, and consequently an increase of HO_2^- yield (Fig. 6b, c). For instance, the 1000 μg cm^{-2} loading of the mixed catalyst in 0.1 M LiOH shows a negligible peroxide formation, compared to about 8 and 28% for 400 and 200 μg cm^{-2} loadings, respectively. This demonstrates that the role of loading on activity is significant. The decrease of the HO_2^- yield with increased loading may be due to the higher chance for an HO_2^- ion for being further reduced to OH^- before diffusing out of the catalyst layer, as suggested in [62] (30 to 130 μg cm^{-2} loading range there). Another possibility (more probable) is that for low loadings, large parts of the GC substrate are uncovered, and at these parts, O_2 reduction follows a 2e-mechanism (this may also be true for [62]). Lower onset potentials and higher current densities for OER were also observed for higher loading of 1 mg cm^{-2}. Furthermore, the kinetic currents (iR-corrected) were calculated for different loadings from the thin film RRDE experiments of Fig. 6a and were used to establish Tafel plots as shown in Fig. 6c. Tafel plots are almost parallel with a Tafel slope of ca. 95 and 160–170 mV dec^{-1} at low and high overpotentials, respectively. The kinetic current density increases as the loading increases until a uniform thin layer covering the GC substrate is reached, which is important for reasonable RRDE analysis.

Moreover, the activity of the mixed catalyst for ORR/OER in two different electrolyte concentrations has also been studied, see Fig. 6a. For ORR, the current densities decrease as the LiOH concentration increases due to the reduced O_2-solubility. The obtained Tafel slopes are similar and have a value of ca. 90–100 mV dec^{-1}, indicating no change in the ORR mechanism in the two solutions, Fig. 6c. The results showed also that the overall electron transfer numbers in ORR did not alter much with electrolyte concentration and

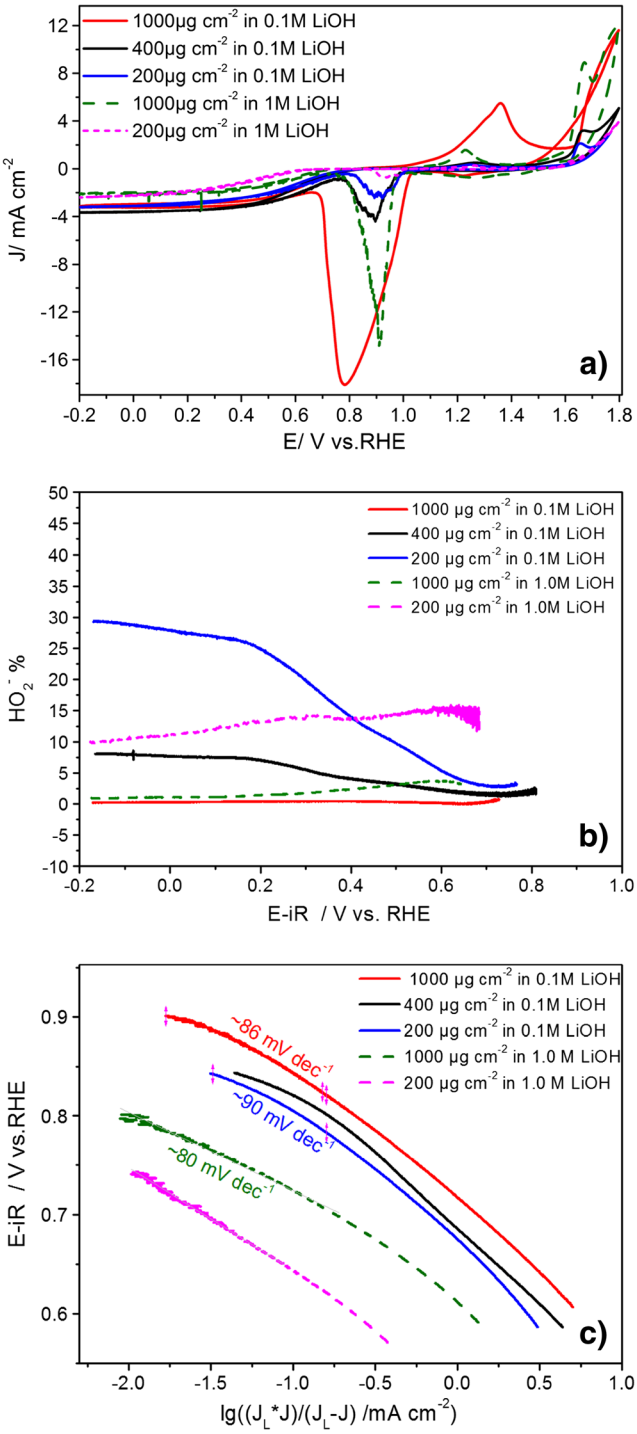

Fig. 6 **a** Polarization curves obtained in O_2-saturated LiOH solution with 10 mV s^{-1} and at 960 rpm for Ag311 + Co_3O_4 (10 wt%) catalyst with 200, 400, and 1000 μg cm^{-2} loadings. **b** The corresponding H_2O^- % obtained when the ring was kept at 1.2 V. **c** Mass-transport corrected Tafel plots obtained from the polarization curves of Fig. 6a

were all close to 4 for 1000 μg cm^{-2} loading. The peroxide species yields were as well comparable and very small (<2% for 1 mg cm^2) over the entire potential range in different concentrations, suggesting a four-electron pathway for ORR at this catalyst, Fig. 6b.

Discussion

To evaluate the overall bifunctionality of the catalysts, the potential difference (ΔE) between ORR at −1.5 mA cm^{-2} and the OER at 4 mA cm^{-2} was calculated and is listed in Table 2. The smaller the potential gap, the more reversible is the oxygen reaction and the better the bifunctional activity. ΔE for our mixed catalyst was 0.99 V at these current densities; however, a value of 0.85 V was obtained at 1 mA cm^{-2}. These ΔEs fall into the lowest values observed for the excellent Pt-free catalysts; however, it is slightly higher than that of Pt/C. The electrochemical parameters for ORR and OER of the as-prepared catalyst are compared to the best carbon-free bifunctional catalysts in literature, as displayed in Table 2. Based on some electrochemical parameters, which reflect the bifunctional activity, it is clear that the mixed catalyst (10%) has a superior activity to OER and comparable activity for ORR to the commercial Pt. Also, this carbon-free mixed catalyst exhibited similar onset potentials for ORR and OER to that of $Li_xCo_2O_2$ loaded on carbon [25]. Thus, Ag + Co_3O_4 (10%) catalyst prepared by simple mixing showed competitive bifunctional activity.

Thus, an interaction between Ag and Co_3O_4 leads to a synergistic effect and improvement in the catalytic activity for both OER and ORR. As demonstrated by the determination of the accessible Ag surface area by Pb-UPD, for ORR, this effect is far beyond what might be expected by simply adding the activities of both components. Our XPS results showed that a reduction of the Co_3O_4 to $Co(OH)_2$ is only achieved when an intimate contact between Ag and the Co-oxide was given, suggesting a catalytic effect of Ag on the redox switching in the Co-oxide. On the other hand, the increased charge of the Ag-oxide peaks in the mixed catalyst indicates as well a catalytic effect of the Co_3O_4 on the oxidation of Ag. It can be anticipated that this mutual catalysis of the redox switching plays a role in the synergistic effect for OER and ORR of the two catalysts.

As in part already discussed in our previous paper [36], possible reasons for this synergetic interaction are as follows:

a) Agglomeration of the particles, particularly of Ag, is prevented or at least reduced when they are covered by Co_3O_4 particles, which leads to a better distribution of the particles and a larger surface area.
b) From SEM images, Ag particles are rougher after several electrochemical cycles. This roughened surface seems to remain stable, which might be due to a stabilization of the

Table 2 Summary of the activity parameters for ORR and OER at our mixed catalyst and other catalysts reported in literature

Catalyst material	Electrolyte	ORR				OER				
		$E_{1/2}/V_{RHE}$	Onset Pot./V_{RHE}	J/mAcm^{-2} at 0.8 V_{RHE}	Tafel slope at low overpot./mV dec^{-1}	E/V at 1.5 mA cm^{-2}	Onset Pot./V_{RHE}	J/mA cm^{-2} at 1.7 V_{RHE}	Tafel slope	E/V at 4 mA cm^{-2}	$\Delta E/V$
Ag311	0.1 M LiOH	0.65	~0.87	0.11	90	0.61	>1.65*	1.1	–	>1.8	>1.19
Co_3O_4	0.1 M LiOH	0.33	~0.71	0.00	~180	0.24	~1.55*	4.0	~70	1.70	1.46
Ag311 + Co_3O_4 (10 wt%)	0.1 M LiOH	0.65	~0.91	0.22	92	0.65	~1.55*	6.5	~115	1.64	0.99
$Ba_{0,9}Co_{0,5}Fe_{0,4}Nb_{0,1}O_{3,\delta}$ [33]	0.1 M KOH	0.64	0.75	Nil	–	0.65	1.55	6.2	–	1.63	0.98
Ag–MnO_2 [34]	0.1 M KOH	0.64	~0.85	~0.29	77	0.63	~1.67	0.55	94	1.85	1.22
Ag–Co alloy [35]	0.1 M NaOH	~0.81	~0.8	2.0	~40	0.82	OER was not reported				
20 wt% Pt/C [36]	0.1 M LiOH	0.87	~1.02	4.35	58	0.91	>1.58	1.67	–	1.77	0.86

* Obtained from DEMS measurements in [36]

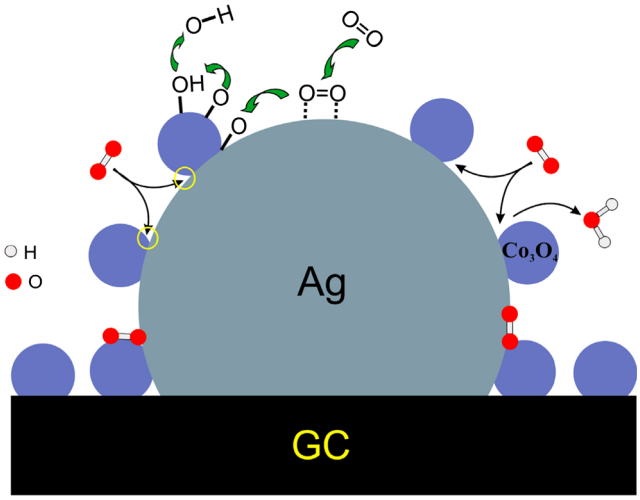

Fig. 7 Schematic illustration of the proposed mechanism of ORR and OER at bifunctional Ag311 + Co_3O_4 mixed catalyst

roughened Ag by Co_3O_4 when they are in contact in the mixture.

c) An electronic effect: the interaction between Ag and Co_3O_4 modifies the electronic properties of the Ag and cobalt oxide and changes the electron density and binding energy. Such an effect often has been reported for bimetallic catalysts [63] and was also reported for combinations of oxides with metals such as in the case of Pt–BSCF oxide [14] Furthermore, cobalt was found to perturb the Ag surface sites in their combination according to DFT and CV methods [20, 35].

d) A spillover mechanism: here for example, Ag facilitates O–O bond breaking, and then the adsorbed oxygen species spills over to Co_3O_4, where the electroreduction takes place, releasing more active sites on Ag surface for further molecules to react. Thus, an improved activity is obtained for ORR. This mechanism is demonstrated in the cartoon shown in Fig. 7. Similarly, for OER, OH^- adsorbs and afterward diffuses to Ag-oxide where OER takes place. Therefore, the two components may be active for two different reaction steps: Ag is predominant in O–O bond splitting in ORR, and Co_3O_4 dominates in the oxidation of water. The combination of two metals for two steps has also been used for the design of bimetallic Pd–Co catalyst for ORR [64].

e) As shown by the XPS results, the presence of Ag facilitates potential-induced redox switching in Co_3O_4 to Co(II) and thus most probably the redox switching as well in the catalytic cycle during OER and ORR similar to the case of Pt with MoO_x [65] or in other oxides [53, 54]. On the other hand, the presence of Co leads not only to an increased stability of the silver oxide, as shown by the shift of the silver oxide reduction peak to a lower potential in the mixed catalyst compared to the pure Ag, but also to an increased amount of silver oxide (cf. Fig. 1a, b). This indicates a stronger adsorbed oxygen interaction with Ag in the mixed catalyst. Therefore, Ag catalyzes the redox switching of Co, and Co catalyzes the redox switching of Ag. Consequently, alteration of the adsorption/desorption behavior of oxygen-containing species at the mixed catalyst could contribute to the synergistic effect.

f) The O_2 molecule reacts (or is formed) directly at the interphase boundary line between Ag and Co_3O_4 with a simultaneous binding to both surfaces. Therefore, O_2 dissociation process could have lower reaction barrier on the triple phase boundary (TPB) at mixed catalyst than on the double phase boundary (DPB) at pure Ag. Hence, O_2 molecules prefer being reduced at TPB than on DPB. A partial burying of the Co_3O_4 into the surface leads to an increased interphase boundary.

Conclusions

We presented a simple synthetic strategy for the design of a bifunctional catalyst with promising electrocatalytic activity. A composite of Co_3O_4 with superior OER activity and Ag with superior ORR activity was prepared by ultrasonic mixing. This optimized mixed catalyst showed better activity to ORR than the pure Ag and better activity to OER than Co_3O_4 alone. The surface analysis also revealed the effectiveness of the unique morphology of the composite to oxygen activity. Notably, the addition of only 10 wt% of Co_3O_4 to Ag in the mixture leads to 88% coverage of the Ag surface by the oxide and despite of that leads to a higher activity than pure Ag. The activity improvement could arise from a synergistic effect between Co_3O_4 and Ag, which could originate from redox switching effect, electronic effect, and spillover effect. Silver particles were not only able to offer a synergistic effect by geometrically and electronically modifying the Co_3O_4 in the mixture but also provide a large amount of highly active sites and more three-phase boundaries. XPS showed that the presence of Ag cation in contact with Co_3O_4 facilitates the redox switching in Co_3O_4, which leads to an enhanced catalytic activity. This carbon-free inexpensive composite exhibited good ORR activity, which is not far from that of the most active precious Pt catalyst and superior activity and stability for OER. The facile preparation method and the outstanding performance make our catalyst as a competitive candidate for ORR/OER that could be applied in alkaline fuel cells and metal–air batteries.

Acknowledgements This work was supported by the German Federal Ministry of Education and Research (BMBF) under the framework of "Lu-Li-Strom aus Luft und Li" project (Fkz:03X4624A). H.M. Amin acknowledges the support from MoHE (Egypt) and DAAD (GERLS scholarship).

References

1. B. Scrosati, J. Garche, J. Power Sources **195**, 2419–2430 (2010)
2. D. Safanama, D. Damiano, R.P. Rao, S. Adams, Solid State Ionics **262**, 211–215 (2014)
3. G. Girishkumar, B. McCloskey, A.C. Luntz, S. Swanson, W. Wilcke, The Journal of Physical Chemistry Letters **1**, 2193–2203 (2010)
4. Z.Y. Liu, J.S. Wainright, M.H. Litt, R.F. Savinell, Electrochim. Acta **51**, 3914–3923 (2006)
5. J.S. Spendelow, A. Wieckowski, Phys. Chem. Chem. Phys. **6**, 5094–5118 (2004)
6. K.A. Striebel, F.R. McLarnon, E.J. Cairns, J. Electrochem. Soc. **137**, 3351–3359 (1990)
7. J.B. Henry, A. Maljusch, M. Huang, W. Schuhmann, A.S. Bondarenko, ACS Catal. **2**, 1457–1460 (2012)
8. N. Bogolowski, T. Nagel, B. Lanova, S. Ernst, H. Baltruschat, K. Nagabhushana, H. Boennemann, J. Appl. Electrochem. **37**, 1485–1494 (2007)
9. P.K. Babu, A. Lewera, J.H. Chung, R. Hunger, W. Jaegermann, N. Alonso-Vante, A. Wieckowski, E. Oldfield, J. Am. Chem. Soc. **129**, 15140–15141 (2007)
10. T. Toda, H. Igarashi, H. Uchida, M. Watanabe, J. Electrochem. Soc. **146**, 3750–3756 (1999)
11. V.R. Stamenkovic, B. Fowler, B.S. Mun, G. Wang, P.N. Ross, C.A. Lucas, N.M. Markovic, Science **315**, 493–497 (2007)
12. L.R. Merte, F. Behafarid, D.J. Miller, D. Friebel, S. Cho, F. Mbuga, D. Sokaras, R. Alonso-Mori, T.-C. Weng, D. Nordlund, A. Nilsson, B. Roldan Cuenya, ACS Catal. **2**, 2371–2376 (2012)
13. L. Gan, C. Cui, S. Rudi, P. Strasser, Top. Catal. **57**, 236–244 (2014)
14. Y. Zhu, C. Su, X. Xu, W. Zhou, R. Ran, Z. Shao, Chem. Eur. J. **20**, 15533–15542 (2014)
15. N.I. Andersen, A. Serov, P. Atanassov, Appl. Catal. B Environ. **163**, 623–627 (2015)
16. W. Yang, J. Salim, S. Li, C. Sun, L. Chen, J.B. Goodenough, Y. Kim, J. Mater. Chem. **22**, 18902–18907 (2012)
17. S. Trasatti, *Electrodes of Conductive Metallic Oxides* (Elsevier Scientific Pub.Co, Amsterdam, 1980)
18. Y. Zhan, C. Xu, M. Lu, Z. Liu, J.Y. Lee, J. Mater. Chem. A **2**, 16217–16223 (2014)
19. Q. Tang, L. Jiang, J. Qi, Q. Jiang, S. Wang, G. Sun, Appl. Catal. B Environ. **104**, 337–345 (2011)
20. Y. Wang, X. Lu, Y. Liu, Y. Deng, Electrochem. Commun. **31**, 108–111 (2013)
21. S. Zhuang, K. Huang, C. Huang, H. Huang, S. Liu, M. Fan, J. Power Sources **196**, 4019–4025 (2011)
22. Y. Liang, H. Liang, J. Wang, Y. Zhou, J. Li, T. Wang, H. Regier, Dai. J. Am. Chem. Soc. **134**, 3517–3523 (2012)
23. Y.J. Sa, K. Kwon, J.Y. Cheon, F. Kleitz, S.H. Joo, J. Mater. Chem. A **1**, 9992–10001 (2013)
24. T.Y. Ma, S. Dai, M. Jaroniec, S.Z. Qiao, J. Am. Chem. Soc. **136**, 13925–13931 (2014)
25. T. Maiyalagan, K.A. Jarvis, S. Therese, P.J. Ferreira, A. Manthiram, Nat. Commun. **5**, 3949 (2014)
26. A. Zadick, L. Dubau, N. Sergent, G. Berthome, M. Chatenet, ACS Catal. **5**, 4819–4824 (2015)
27. S. Velraj, J.H. Zhu, J. Electroanal. Chem. **736**, 76–82 (2015)
28. Y. Liang, Y. Li, H. Wang, J. Zhou, J. Wang, T. Regier, H. Dai, Nat. Mater. **10**, 780–786 (2011)
29. J.-J. Han, N. Li, T.-Y. Zhang, J. Power Sources **193**, 885–889 (2009)
30. B.B. Blizanac, P.N. Ross, N.M. Markovic, J. Phys. Chem. B **110**, 4735–4741 (2006)
31. S. Kumar, C. Selvaraj, L.G. Scanlon, N. Munichandraiah, Phys. Chem. Chem. Phys. **16**, 22830–22840 (2014)
32. M. De Koninck, B. Marsan, Electrochim. Acta **53**, 7012–7021 (2008)
33. C. Jin, Z. Yang, X. Cao, F. Lu, R. Yang, Int. J. Hydrog. Energy **39**, 2526–2530 (2014)
34. F.W.T. Goh, Z. Liu, X. Ge, Y. Zong, G. Du, T.S.A. Hor, Electrochim. Acta **114**, 598–604 (2013)
35. A. Holewinski, J.-C. Idrobo, S. Linic, Nat. Chem. **6**, 828–834 (2014)
36. H.M.A. Amin, H. Baltruschat, D. Wittmaier, K.A. Friedrich, Electrochim. Acta **151**, 332–339 (2015)
37. D. Wittmaier, N. Wagner, K.A. Friedrich, H.M.A. Amin, H. Baltruschat, J. Power Sources **265**, 299–308 (2014)
38. D. Wittmaier, N.A. Cañas, I. Biswas, K.A. Friedrich, Adv. Energy Mater. **5**, 1500763–1500771 (2015)
39. E. Kirowa-Eisner, Y. Bonfil, D. Tzur, E. Gileadi, J. Electroanal. Chem. **552**, 171–183 (2003)
40. M. Hepel, S. Bruckenstein, Electrochim. Acta **34**, 1499–1504 (1989)
41. G.K.H. Wiberg, K.J.J. Mayrhofer, M. Arenz, Fuel Cells **10**, 575–581 (2010)
42. T.J. Schmidt, H.A. Gasteiger, G.D. Stab, P.M. Urban, D.M. Kolb, R.J. Behm, J. Electrochem. Soc. **145**, 2354–2358 (1998)
43. F. Lu, G.N. Salaita, H. Baltruschat, A.T. Hubbard, J. Electroanal. Chem. **222**, 305–320 (1987)
44. F.H.B. Lima, J.F.R. de Castro, E.A. Ticianelli, J. Power Sources **161**, 806–812 (2006)
45. A. Bergmann, E. Martinez-Moreno, D. Teschner, P. Chernev, M. Gliech, J.F. de Araújo, T. Reier, H. Dau, P. Strasser, Nat. Commun. **6**, 8625 (2015)
46. J. Chivot, L. Mendoza, C. Mansour, T. Pauporté, M. Cassir, Corros. Sci. **50**, 62–69 (2008)
47. M.C. Biesinger, B.P. Payne, A.P. Grosvenor, L.W.M. Lau, A.R. Gerson, R.S.C. Smart, Appl. Surf. Sci. **257**, 2717–2730 (2011)
48. J. Yang, H. Liu, W.N. Martens, R.L. Frost, J. Phys. Chem. C **114**, 111–119 (2009)
49. H. Göhr, A. Breitenstein, Electrochim. Acta **13**, 1377–1388 (1968)
50. A.F. Holleman, E. wiberg, Lehrbuch der Anorganischen Chemie, 33 ed., Walter de Gruyter, Berlin, 1985.
51. C.D. Wagner, W.M. Riggs, L.E. Davis, J.F. Moulder, G.E. Muilenberg, *Handbook of X-Ray Photoelectron Spectroscopy* (Perkin-Elmer Corporation, Eden Prairie, 1979)
52. V.K. Kaushik, J. Electron Spectrosc. Relat. Phenom. **56**, 273–277 (1991)
53. L.I. Krishtalik, Electrochim. Acta **26**, 329–337 (1981)
54. A.C.C. Tseung, S. Jasem, Electrochim. Acta **22**, 31–34 (1977)
55. J.L. Fernández, M.R. Gennero de Chialvo, A.C. Chialvo, Electrochim. Acta **47**, 1145–1152 (2002)
56. Q. Fu, W.-X. Li, Y. Yao, H. Liu, H.-Y. Su, D. Ma, X.-K. Gu, L. Chen, Z. Wang, H. Zhang, B. Wang, X. Bao, Science **328**, 1141–1144 (2010)
57. F. Hernandez, H. Baltruschat, Langmuir **22**, 4877–4884 (2006)
58. Z. Jusys, H. Massong, H. Baltruschat, J. Electrochem. Soc. **146**, 1093 (1999)
59. G. Samjeské, X.-Y. Xiao, H. Baltruschat, Langmuir **18**, 4659–4666 (2002)
60. H. Massong, S. Tillmann, T. Langkau, E.A. Abd El Meguid, H. Baltruschat, Electrochim. Acta **44**, 1379–1388 (1998)
61. J. Suntivich, K.J. May, H.A. Gasteiger, J.B. Goodenough, Y. Shao-Horn, Science **334**, 1383–1385 (2011)
62. T. Poux, A. Bonnefont, G. Kéranguéven, G.A. Tsirlina, E.R. Savinova, ChemPhysChem **15**, 2108–2120 (2014)
63. H. Baltruschat, S. Ernst, N. Bogolowski, in: E. Santos, W. Schmickler (Eds.), Catalysis in Electrochemistry, Wiley, 2011, pp. 297–337.
64. J.L. Fernandez, D.A. Walsh, A.J. Bard, J. Am. Chem. Soc. **127**, 357–365 (2005)
65. R. Vellacheri, S.M. Unni, S. Nahire, U.K. Kharul, S. Kurungot, Electrochim. Acta **55**, 2878–2887 (2010)